Capacity fade in Sn–C nanopowder anodes due to fracture

Katerina E. Aifantis [a,b,*], Tao Huang [a,c], Stephen A. Hackney [a,d], Thapanee Sarakonsri [a,e], Aishui Yu [a,c]

[a] Lab of Mechanics and Materials, Aristotle University, Thessaloniki 54124, Greece
[b] Physics, Michigan Technological University, Houghton 49931, USA
[c] Institute of New Energy, Fudan University, Shanghai 200438, China
[d] Materials Science and Engineering, Michigan Technological University, Houghton 49931, USA
[e] Chemistry, Chiangmai University, Chiangmai, Thailand

ARTICLE INFO

ABSTRACT

Sn based anodes allow for high initial capacities, which however cannot be retained due to the severe mechanical damage that occurs during Li-insertion and de-insertion. To better understand the fracture process during electrochemical cycling three different nanopowders comprised of Sn particles attached on artificial graphite, natural graphite or micro-carbon microbeads were examined. Although an initial capacity of $700\,mAh\,g^{-1}$ was obtained for all Sn–C nanopowders, a significant capacity fade took place with continuous electrochemical cycling. The microstructural changes in the electrodes corresponding to the changes in electrochemical behavior were studied by transmission and scanning electron microscopy. The fragmentation of Sn observed by microscopy correlates with the capacity fade, but this fragmentation and capacity fade can be controlled by controlling the initial microstructure. It was found that there is a dependence of the capacity fade on the Sn particle volume and surface area fraction of Sn on carbon.

© 2011 Elsevier B.V. All rights reserved.

1. Introduction

Both Sn and Si are highly reactive with respect to Li, giving capacities of $996\,mAh\,g^{-1}$ and $4200\,mAh\,g^{-1}$ [1], respectively, upon maximum Li-insertion. They cannot be used, however, in their pure form as anodes due to the 300% volume expansion they experience upon the formation of Li alloys. This volume expansion and sub-sequent contraction, upon Li de-insertion, results in severe mechanical damage, which corresponds to capacity fading during cycling. After the first 20 cycles, therefore, it is possible for the capacity of Sn nanoparticles to drop to $210\,mAh\,g^{-1}$ [2], which is even lower than that of commercially used graphite ($372\,mAh\,g^{-1}$ [3]).

Deformation is less severe at the nanoscale so keeping the particle size in the nm range is common practice for battery developers [4,5]. Furthermore, mechanical damage of Si and Sn can be significantly reduced by embedding them in a matrix that can buffer/constrain their expansion during electrochemical cycling; an overview can be found in [6]

Particularly, embedding 25 nm Si nanoparticles in carbon allowed for capacities of $1000\,mAh\,g^{-1}$ to be retained for 30 cycles

[7]. For Sn-based anodes, stable capacities of $500\,mAh\,g^{-1}$ have been achieved by embedding Sn nanoparticles in carbon [8]. In order to achieve such high capacities the Sn content had to be 50 wt%. A different type of Sn–C microstructure that can provide capacities that are greater than that of the C matrix is that of attaching Sn particles on carbon surfaces. In [9] the capacity of Vulcan C was increased 85% by attaching 8 wt%Sn as SnO_2 islands with diameters between 5 and 20 nm. Unfortunately, Vulcan is a low capacity carbon ($180\,mAh\,g^{-1}$) and, therefore, it cannot provide high capacity anodes. In a previous study, in which Sn was attached on the surface of a higher capacity synthetic graphite, significant capacity fade was observed and after 20 cycles it had dropped below $400\,mAh\,g^{-1}$ [10].

Microstructural studies of cycled Sn-on-carbon electrode materials are very limited and there appears to be little quantitative data relating the microstructure of these materials to their capacity fade. This paper contributes to closing this gap in understanding, by using transmission and scanning electron microscopy (TEM & SEM) to examine the microstructural changes during electrochemical cycling and the dependence of capacity fade on the Sn particle configuration for three different Sn–C materials. Natural graphite, artificial graphite and microcarbon–microbeads with capacities of $350\,mAh\,g^{-1}$ (Shandong Carbon Materials Ltd., China) was employed as the base material onto which the Sn was attached. Sn deposition on all the carbons was carried out using the fabrication method described in [11]. TEM and SEM were performed

* Corresponding author at: Lab of Mechanics and Materials, Aristotle University, Thessaloniki 54124, Greece. Tel.: +30 6936208504; fax: +30 2310 995921.
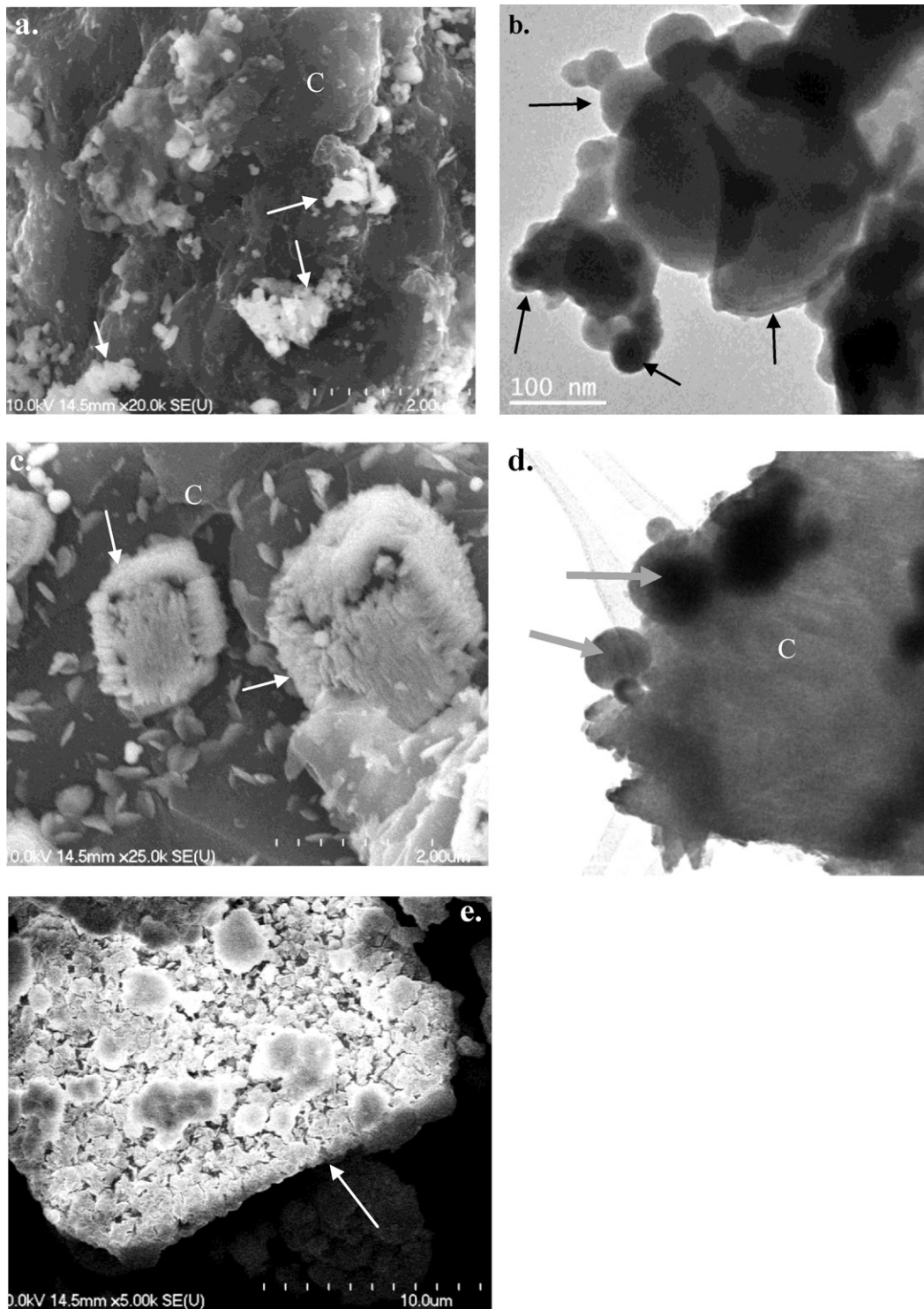E-mail address: k.aifantis@mom.gen.auth.gr (K.E. Aifantis).

Fig. 1. Microstructure of as prepared Sn–C nanopowders: (a) SEM image of Sn–MCMB; (b) TEM image of Sn–MCMB; (c) SEM image of Sn-artificial graphite; (d) TEM image of Sn-artificial graphite; (e) SEM image of Sn-natural graphite. In the SEM images the Sn and SnO_2 appear bright, whereas in the TEM images they appear black. All of the Sn rich particles shown here are attached to carbon particles, indicated as C. Arrows indicate the Sn and SnO_2 particles.

after long term cycling to observe the mechanical damage that took place upon continuous Li-insertion and de-insertion through measurement of Sn particle sizes.

To further, document fracture upon Li-insertion, cells were interrupted at various stages of the first and second electrochemical cycles and post mortem TEM/SEM was performed, documenting "significant fracture" of the Sn islands during the first cycle.

2. Experimental procedure

The fabrication method employed was that described in [11], according to which $SnCl_4$ is reduced on the surface of carbon or graphite. Depending on the carbon used the microstructure differed significantly. Particularly, it is seen in the SEM and TEM images of Fig. 1 that when MCMB carbon (Fig. 1a,b) and artificial graphite (Fig. 1c,d) were employed the islands had a diameter in

both the nanometer and micrometer scale (bimodel size distribution), whereas when natural graphite was used the Sn covered the whole surface as a thin layer (Fig. 1e). It should be noted that XRD indicated that when MCMB was used the Sn attached in the form of Sn metal and SnO_2, whereas on the graphites (artificial and natural) only pure Sn was attached [11]. The Sn content present in all the composites was determined through thermogravimmetry to be 43.2 wt%Sn for Sn–MCMB, 40.9 wt%Sn for Sn–NG and 42.1 wt%Sn for Sn–AG.

In order to test the applicability of these Sn–C nanopowders as anodes the working electrode was prepared by coating slurries of active material and polyvinylidene fluoride (PVDF) with a weight ratio of 90:10, using 1-methyl-2-pyrrolidinone (NMP) as the solvent onto a copper foil. The electrolyte was 1 M $LiPF_6$ dissolved in a mixed solvent of ethylene carbonate (EC) and dimethyl carbonate (DMC) (1:1 in weight), and a microporous polypropylene film (Celgard 2300) was used as the separator. The galvanostatic charge–discharge tests were performed on a battery test system (Land CT2001A, Wuhan Jinnuo Electronic Co. Ltd., China) at a constant current density of $50\,mA\,g^{-1}$ in the potential range from 0 to 2.5 V (vs. Li^+/Li). For comparison purposes, MCMB, artificial graphite and natural graphite, prior to the Sn attachment, were also tested as anodes under the same conditions.

The SEM analysis was performed in a Hitachi S-4700 FESEM, using a cold field emission filament and an accelerating voltage of 10 kV. The TEM analysis was done in a JEOL JEM-6400FX TEM using a lanthanum hexaboride (LaB_6) filament and an accelerating voltage was set at 200 kV.

3. Results

3.1. Long term cycling

Fig. 2 shows the cyclability of the graphites prior to the attachment of Sn. Fig. 3 illustrates the capacity obtained by cycling the as prepared Sn–C materials shown in Fig. 1. The initial capacity for all Sn–C nanocomposites is approximately, between 700 and $800\,mAh\,g^{-1}$, for all cases. This high capacity is attributed to the Sn, which gives capacities of $900\,mAh\,g^{-1}$. With continuous cycling, though, a significant capacity fade occurred. This fade was anticipated to some extent for the MCMB and the natural graphite, since it was observed prior to the Sn attachment as well (Fig. 1). For the artificial graphite, however, this capacity fade was entirely due to the presence of the attached Sn islands. It is well known that Sn fractures from the first Li-insertion [12] and, therefore, severe fracture was expected during long term cycling for
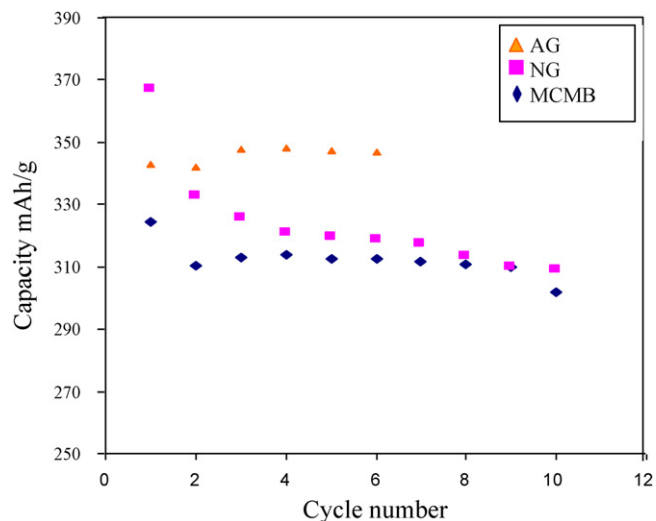

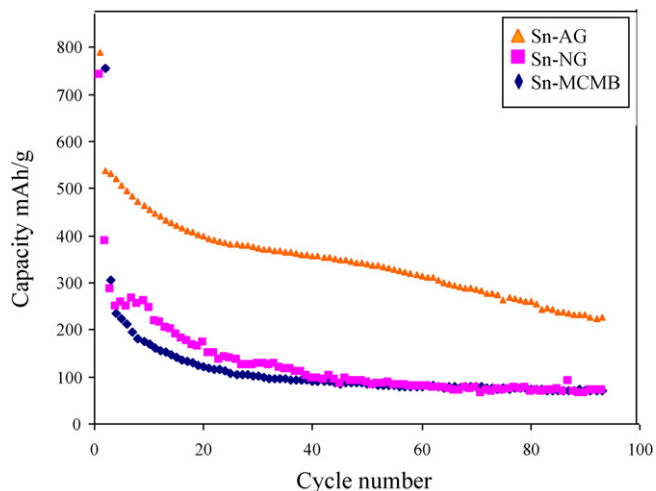**Fig. 2.** Capacity retention in graphites prior the attachment of Sn at a current density of $50\,mA\,g^{-1}$.

Fig. 3. Electrochemical cycling of Sn–C nanopowders at a current density of $50\,mA\,g^{-1}$.

all the Sn-graphite anodes. To verify this SEM and TEM were performed after long term cycling, and it was verified that the Sn or SnO_2 islands had fractured into multiple nanoparticles, as seen in Fig. 4, resulting into a disruption of connectivity and loss of active
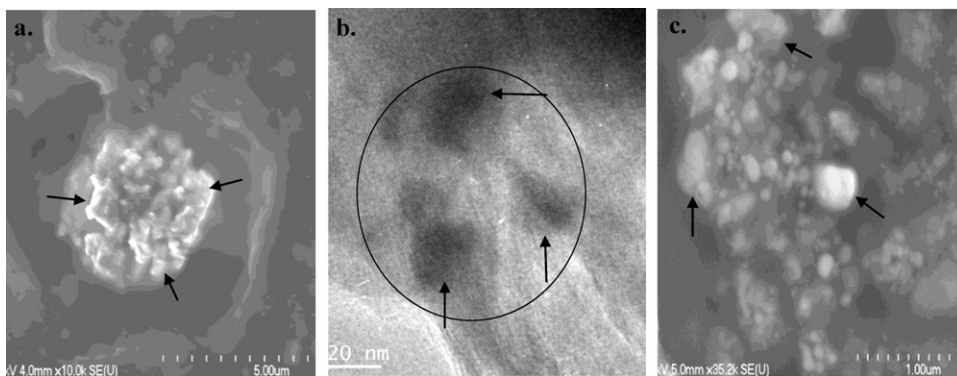

Fig. 4. Fracture observed after cycling: (a) SEM image for SnO_2–MCMB; (b) TEM of Sn–AG, (c) SEM of Sn–NG. Arrows indicate the Sn. The fragmented Sn particles comprised a single Sn island before Li-insertion. In image (b) for example the ~20 nm fragmented particles, enclosed in the circle, comprised a Sn island of approximately 100 nm as seen in Fig. 1d; modified from [15].
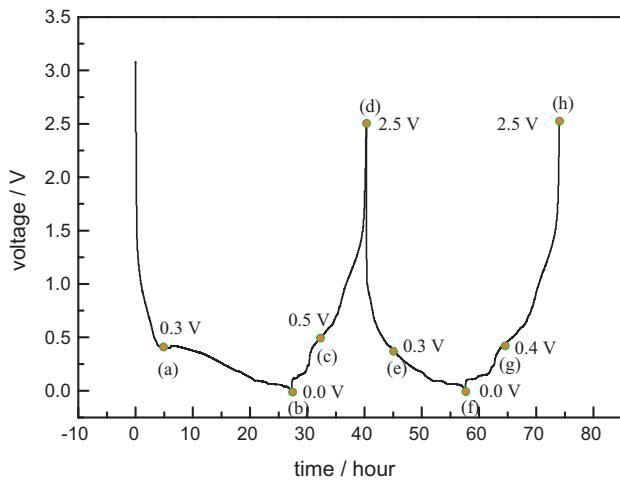
Fig. 5. First two electrochemical cycles for Sn–NG.

Fig. 7. First two electrochemical cycles of Sn/AG nanopowder.

materials into the electrolyte and hence a continuous fade in the capacity.

3.2. Fracture during initial cycling

Electrochemical cycling was stopped at various stages during the first two cycles for Sn–AG and Sn–NG, and post mortem TEM was performed.

Fig. 5 depicts the first two electrochemical cycles of the Sn–NG anode. Performing TEM during the first partial lithiation (Fig. 6) indicated that even at this early lithiation stage the Sn layer that covered the natural graphite crumbled into multiple nanoparticles, resulting into the significant capacity loss observed in the second cycle of Fig. 3.

Since the Sn–AG shows significant fade on the first cycle, the microstructural changes during the first discharge (Fig. 7) were examined in more detail in Fig. 8. Fig. 8a–f shows the microstructural evolution as a function of discharge-charge level. Small particles of Sn rich material are observed near the surface of larger particles, and the number density of the small particles appears to increase with depth of discharge. The stages at which the TEM images were taken are indicated in Fig. 7.
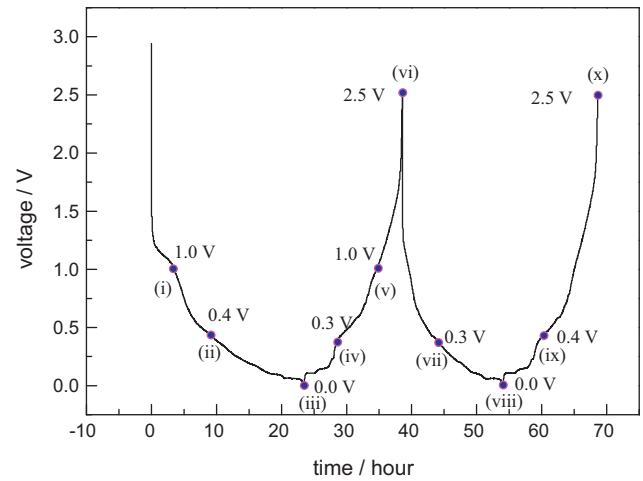
4. Discussion

Fig. 3 illustrates that the greatest capacity loss took place during the first cycle for all three materials. For Sn/SnO$_2$–MCMB this can be partially attributed to the fact that some Li-ions are lost in the irreversible formation of Li$_2$O during the first Li-insertion [13] since SnO$_2$ in addition to Sn metal were attached on the MCMB for this case. For Sn-artificial graphite and Sn-natural graphite, however, this high irreversible capacity loss is anticipated to be solely due to the fracture of the Sn islands.

Fracture of electrode materials due to volume changes throughout the electrochemical cycle has been previously considered. For freestanding particles, the fracture of large volume change materials such as Sn has been described as a function of the volume of the particle [14]. For particles attached to substrates, as in Sn attached to C, mechanics methodologies have been used to predict the delamination process as a function of aspect ratio [12]. The severe fracture observed during initial Li-insertion in Sn–NG (Fig. 6) was expected from these theoretical predictions. By using theoretical mechanics it was shown [12] that when the aspect ratio (height/width) of the Sn particles attached on the carbon is less than 0.3, delamination of the Sn occurs upon Li-insertion, and indeed in Fig. 6, it is seen that the previously continuous Sn layer
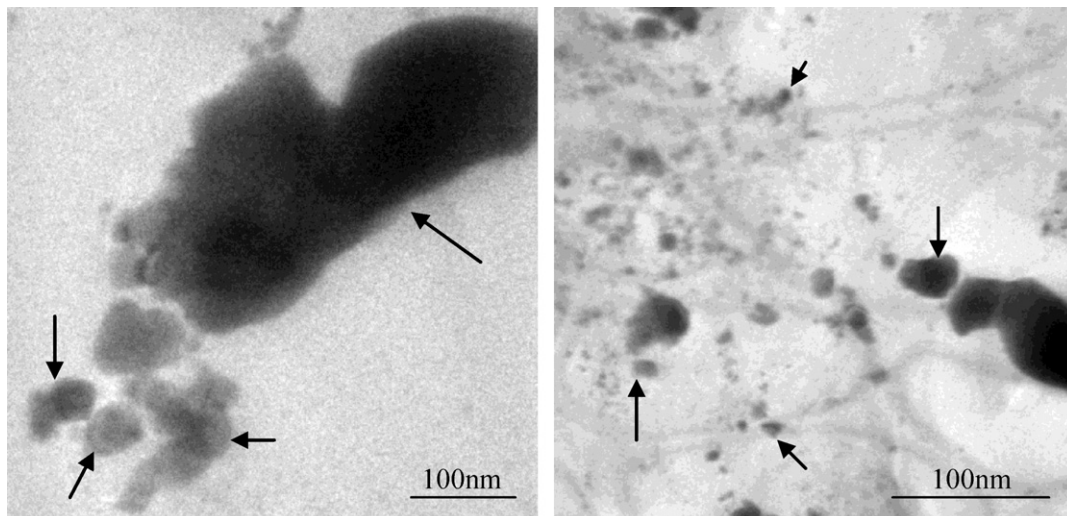

Fig. 6. Microstructure at stage (a) of Sn–NG cycle in Fig. 5. Very small Sn particles detached from the carbon are observed. The Sn appears in shades of grey. Arrows point at some indicative fractured Sn particles; modified from [15].
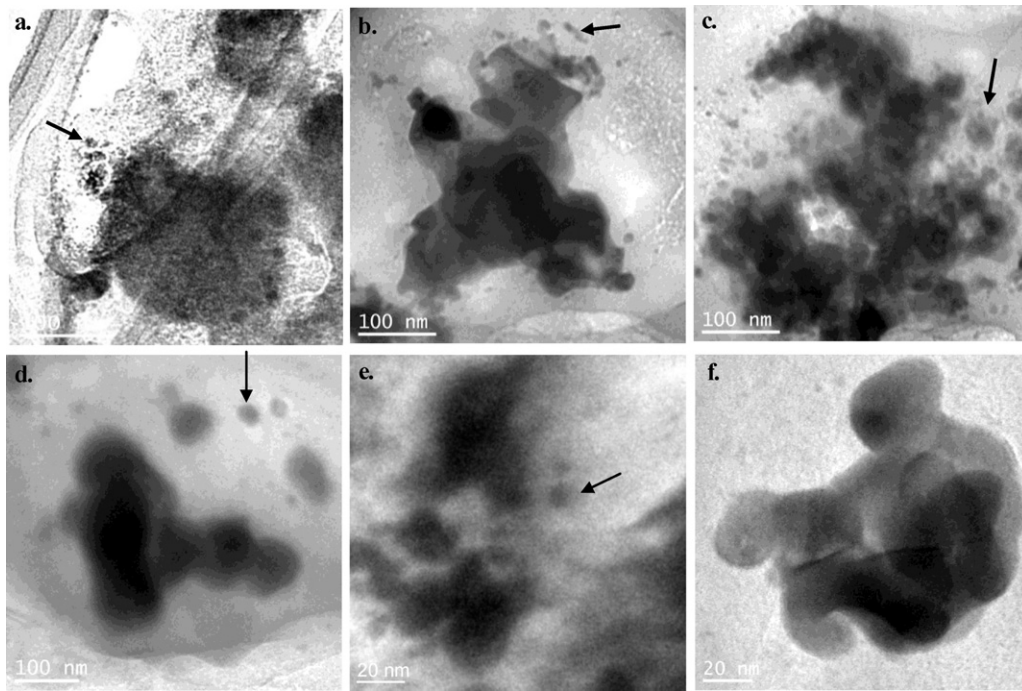
Fig. 8. The observation of small Sn particles in close proximity to the surface of larger Sn particles is interpreted as an indication of fracture during various stages indicated in Fig. 6: (a) taken at stage i, (b and c) taken at stage iii, (d) taken at stage v, (e and f) taken at stage viii. For (f) no fractured particles are observed which might imply that they had completely detached and diffused into the electrolyte; modified from [15].

(height/width ≪ 0.3) is replaced by fragmented nanoparticles. In addition to particle size and aspect ratio, the spacing of the Sn particles on the carbon is of significance to the total elastic strain energy density of the system. In this work, the concepts of particle volume, shape and spacing relating to particle fracture and particle delamination are brought together by measuring both the Sn particle volume and Sn particle area fraction on the carbon. Considering a cylindrical geometry it is deduced that for a particle of height h and width $2r$, the Sn particle volume (V) is

$$V = h\pi r^2 \qquad (1)$$

with an aspect ratio (A_s) of $A_s = h/2r$. If the cylindrical Sn particle is centered on a circular area of the carbon surface πR^2 giving a particle spacing of $2R$, then the area fraction (F) is

$$F = \frac{\pi r^2}{\pi r^2 + \pi R^2} = \frac{h^2}{4A_s^2 R^2 + h^2}. \qquad (2)$$

Thus for a given particle volume, the area fraction on the substrate is seen to be an important reflection of the aspect ratio and spacing of the Sn particles. In Table 1 the area fraction and average volume of the Sn islands are reported.

It is therefore, of interest to develop an empirical expression that can relate the capacity retention of Sn/C anodes to their initial microstructure. In doing so a normalized capacity, N_c, is defined as

$$N_c = \frac{1}{C_1} \sum_{n=1}^{n=25} C_n, \qquad (3)$$

Table 1
Normalized capacity, volume average and area fraction for various anodes; modified from [15].

Anode	Normalized capacity	Volume average (μm^3)	Area fraction
Sn/NG	7.23	2.69	0.74
Sn/AG	13.69	2.78	0.42
Sn/MCMB	5.43	12.53	0.55

where C_1 is the capacity of the first cycle and C_n is the capacity of the nth cycle. If a capacity decay was not observed then Eq. (3) would give $N_c = 25$. However, depending on the magnitude of the area fraction (A) and average volume (V) of the Sn or SnO$_2$ islands, N_c, decreases. An empirical way to capture this decrease is to subtract A and V from 25 as follows:

$$N_c = 25 - aA - bV - c\sqrt{A}, \qquad (4)$$

where a, b, and c are constants, which are computed by substituting the values of Table 1 into Eq. (4) and solving the three equations simultaneously. Particularly, it is found that $a = 18.25$, $b = 0.57\ \mu m^3$, $c = 3.16$. Eq. (4) can, therefore, be plotted in Fig. 9 to illustrate how the capacity depends on the initial microstructure of the anode. Hence, according to the experimental data, Eq. (4) predicts that the capacity retention is better when A and V are kept at low values.

Based on Fig. 9, the most optimum microstructure is that of nanosized islands that are spaced sufficiently apart. This prediction is in agreement with the experimental data reported in [9] for SnO$_2$ islands attached on amorphous Vulcan C. These anodes showed 100% capacity retention after the first cycle which showed the expected decrease due to loss of Li to form Li$_2$O. The area fraction of the SnO$_2$ was 0.32 and the volume average of the SnO$_2$ was 34 nm^3 [15], insertion of these values in Eq. (4) estimated a value for $N_c = 17.37$ (indicated in Fig. 9), which is significantly higher than that of the materials studied in the present article with much higher values for A and V. Hence, Eq. (4) can successfully predict the performance of Sn/C nanostructured anodes, once their microstructure is known.

In addition to the information that the SEM and TEM images provide about the optimum microstructure of Sn/C anodes, the TEM images also provide information about the critical particle size that the Sn fractures into. Fig. 3 and Table 1 show that Sn/AG is the most promising of the materials examined herein. Fig. 8 showed that severe fracture of the Sn occurred during the first two electrochemical cycles, during which the 100 nm Sn islands fractured into 20 nm particles. Fig. 4b which was taken after long term cycling
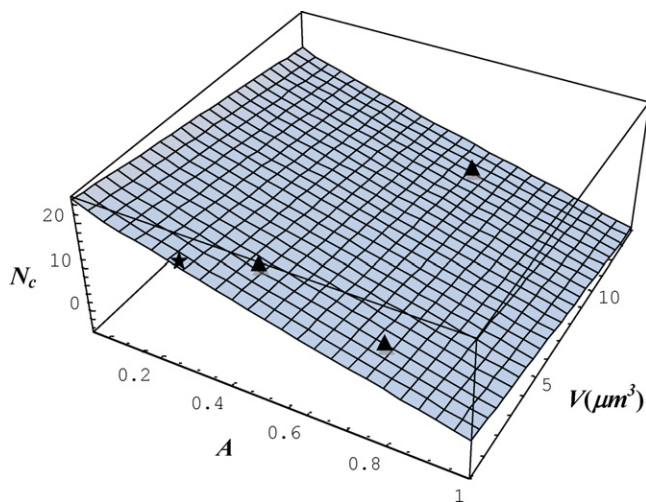
Fig. 9. Normalized capacity as a function of area fraction and average volume size. The actual points of Table 1 are indicated as triangles, while the Sn-Vulcan data are shown with a star, for comparison.

Fig. 10. Comparing capacity curves of Sn/NG and NG.

showed that after continuous cycling the fractured Sn particles retained their size of 20 nm, suggesting that once the Sn became 20 nm it could not easily fracture further. Therefore, the optimum particle size of the initial Sn/C microstructure would be Sn islands below 20 nm, in order to avoid fracture. This provides an additional explanation of the unique electrochemical performance observed for SnO_2/Vulcan in [9] since the SnO_2 islands were between 5 and 20 nm, and hence most likely did not fracture and allowed for a constant capacity retention for 400 cycles.

A more detailed description regarding the SEM and TEM of the lithiated materials can be found in [15].

A final issue that must be addressed is the fact that the capacity of the Sn/MCMB and Sn/NG anodes after long term cycling, shown in Fig. 3, dropped below 300 mAh g^{-1}, which is the capacity of the carbon base (Fig. 2). This result is problematic because the Sn/C electrode is expected to behave as a two phase system, where the cycling performance of the Sn is additive to the discharge performance of the C. A contribution to this loss in capacity is expected from the fracture of Sn, causing detatchment of the active material from the electrode. However, this cannot account for the entire drop in specific capacity. In order to further examine the underlying processes that occur with continuous cycling, the charge/discharge voltage:capacity curves for NG and Sn–NG (50 cycles) are compared in Fig. 10. It is apparent that the extensive low voltage capacity of the NG is not observed in the aged Sn–NG and that the Sn–NG voltage hysteresis is significantly larger than the NG hysteresis. These observations are examined here using the Thevenin equivalent circuit model [6]. In the Thevenin model, the observed voltage, V, is a function of the open circuit voltage, OCV, the current, I and the internal resistance for charge and discharge, R_{ch} and R_{dis}. According to this model, the magnitude of the hysteresis in a constant current discharge is $[|I| (R_{dis} + R_{ch})]$. Thus, the large hysteresis in the Sn–NG voltage:capacity curve does suggest a large internal resistance as defined by the Thevenin equivalent circuit model. On discharge, the observed voltage in the Thevenin model is

$$V = OCV - |I|R_{dis}. \tag{5}$$

The measurement of discharge capacity is terminated as the voltage approaches zero, which implies the current and internal resistance can influence the magnitude of the specific capacity. That is, if the OCV is small as in the extended tail of the NG discharge, the $[|I| R_{dis}]$ term could drive the voltage to zero at a capacity significantly below the theoretical maximum, and thus
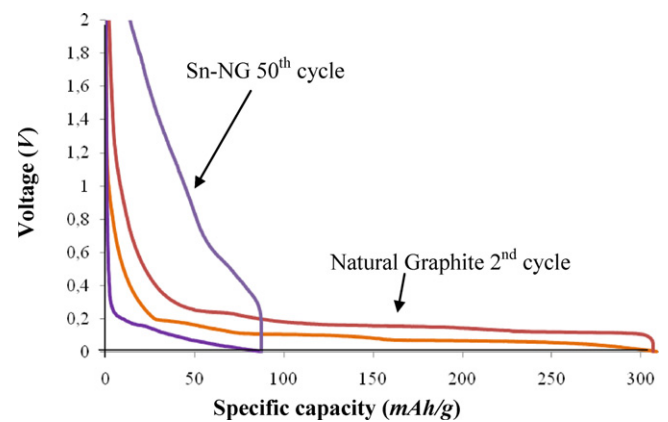
prematurely truncate the discharge process. It is proposed that Fig. 10 is consistent with this concept, as the large hysteresis in the Sn–NG anode is coupled with a relatively steep, negative slope in the discharge curve at the intercept with the capacity axis. This implies that the carbon component of capacity that occurs at small OCV with small negative slope in the discharge curve is not being measured because the $[|I| R_{dis}]$ term has driven this component of the capacity below the zero voltage line.

5. Conclusions

In the present study a detailed analysis was performed to study the fracture of Sn-based anodes that comprise of Sn or SnO_2 islands attached on artificial graphite, natural graphite and MCMB. SEM and TEM images illustrated that all Sn–C materials experienced severe fracture during long term cycling, while observing in more detail the first two electrochemical cycles it was seen that severe fracture occurs during the first lithiation. Particularly, it was shown that upon Li-insertion the Sn islands crumble. The amount of capacity fade can be related to the experimental measurement of initial area fraction and volume average of the Sn islands using an empirical approach. The resulting empirical equation predicts that the smaller these quantities become, the higher the capacity retention. The attachment of Sn on the C results in an increase in the magnitude of the voltage hysteresis, which can be interpreted as an increase in internal resistance of the electrode. A significant component of the observed Sn/C capacity fade is suggested to occur because of internal resistance induced truncation of the constant current discharge.

Acknowledgment

References

[1] L.Y. Beaulieu, K.W. Eberman, R.L. Turner, L.J. Krause, J.R.J.R. Dahn, Electrochem. Solid State Lett. 4 (2001) A137.
[2] Z. Wang, W. Tian, X. Li, J. Alloys Compd. 439 (2007) 350.
[3] R.R. Fong, U. von Sacken, J.R. Dahn, J. Electrochem. Soc. 137 (1990) 2009.
[4] H. Li, X.J. Huang, L.Q. Chen, Z.G. Wu, Y. Liang, Electrochem. Solid State Lett. 2 (1999) 547.
[5] H. Li, X.J. Huang, L.Q. Chen, G.W. Zhou, Z. Zhang, D.P. Yu, Y.J. Mo, Solid State Ionics 135 (2000) 181.
[6] K.E. Aifantis, S.A. Hackney, V.R. Kumar (Eds.), High Energy Density Li-ion Batteries, Wiley-VCH, 2010.
[7] Z. Wen, X. Yang, S. Huang, J. Power Sources 174 (2007) 1041.
[8] G. Derrien, J. Hassoun, S. Panero, B. Scrosati, Adv. Mater. 19 (2007) 2336.

[9] K.E. Aifantis, S. Brutti, T. Sarakonsri, B. Scrosati, Electrochim. Acta 55 (2010) 5071.
[10] L. Balan, R. Schneider, J. Ghanbaja, P. Willmann, D. Billaud, Electrochim. Acta 51 (2006) 3385.
[11] K.Adpakpang, T. Sarakonsri, K.E. Aifantis, S.A. Hackney, submitted for publication.
[12] K.E. Aifantis, S.A. Hackney, J. Power Sources 196 (2011) 2122.
[13] Y. Idota, T. Kubota, A. Matsufuji, Y. Maekawa, T. Miyasaka, Science 276 (1997) 1395.
[14] J. Wolfenstine, D. Foster, J. Read, W.K. Behl, W. Luecke, J. Power Source 87 (2000) 1.
[15] M. Hayock, K.E. Aifantis, P. Sanders, S.A. Hackney, Mater. Sci. Eng. A, doi:10.1016/j.msea.2011.08.060.